Eur. Phys. J. D **5**, 145–157 (1999)

THE EUROPEAN PHYSICAL JOURNAL D
EDP Sciences

Quasiclassical dynamics of resonantly driven Rydberg states

A. Buchleitner[1,a], K. Sacha[2], D. Delande[3], and J. Zakrzewski[2]

[1] Max-Planck-Institut für Quantenoptik, Hans-Kopfermann-Str. 1, 85748 Garching, Germany
[2] Instytut Fizyki imienia Mariana Smoluchowskiego, Uniwersytet Jagielloński, ulica Reymonta 4, 30-059 Kraków, Poland
[3] Laboratoire Kastler-Brossel, tour 12, étage 1, 4 place Jussieu, 75252 Paris Cedex 05, France

Received: 23 June 1998 / Accepted: 10 November 1998

Abstract. We present a semiclassical analysis of the dynamics of Rydberg states of atomic hydrogen driven by a resonant microwave field of linear polarization. The semiclassical quasienergies of the atom in the field are found to be in very good agreement with the exact quantum solutions. The ionization rates of individual eigenstates of the atom dressed by the field reflect their quasiclassical dynamics along classical periodic orbits in the near integrable regime, but exhibit a transition to nonspecific rates when global chaos takes over in phase space. We concentrate both on the principal resonance where the unperturbed Kepler frequency ω_K is equal to the driving field frequency ω and on the higher primary resonance $\omega = 2\omega_K$. The latter case allows for the construction of nondispersive wave packets which propagate along Kepler ellipses of intermediate eccentricity.

PACS. 05.45.+b Theory and models of chaotic systems – 32.80.Rm Multiphoton ionization and excitation to highly excited states (e.g., Rydberg states) – 42.50.Hz Strong-field excitation of optical transitions in quantum systems; multi-photon processes; dynamic Stark shift

1 Introduction

The dynamics of atomic Rydberg states under external periodic driving have been under intensive study for more than two decades [1,2]. The surprising experimental observation [1] of the efficient excitation and ionization of Rydberg states by an electromagnetic field of frequency comparable to the Rydberg level spacing led to the interpretation of this process in terms of the underlying *chaotic* classical dynamics of the driven Rydberg electron [3]: although a single trajectory is perfectly deterministic, the global motion – when averaged over initial conditions – is similar to a diffusive motion, leading to excitation and eventually "chaotic" ionization of the Rydberg electron. Hence, microwave driven Rydberg states had been identified as *the* prototype of atomic systems which allow for the direct monitoring of the temporal evolution of a quantum system with a classically chaotic counterpart. Due to the explicit time dependence of the excitation and ionization processes, quantum limitations of the global, classically chaotic transport, nowadays known under the term "dynamical localization", have been predicted and experimentally verified [3–8]. However, further experimental evidence has suggested that besides global features of the quantal transport process, there are signatures of local structures in classical phase space emerging from experimental ionization threshold values [9]. The theory of dynamical localization ignores stable islands in phase space that protect the classical electron from wandering towards the ionization threshold; apparently, these islands are responsible for an increased value of the driving field amplitude needed to ionize the atom when prepared in an appropriate initial atomic state [10].

The largest of these stable structures in phase space is created by the principal resonance between the driving field and the (fundamental harmonic of the) unperturbed Kepler motion of the Rydberg electron. In terms of the principal quantum number n_0 of the initial atomic state, the Kepler frequency $\omega_K = n_0^{-3}$ has to be matched by the driving frequency ω, *i.e.* $\omega n_0^3 \simeq 1$. Indeed, for fixed ω, the experimental ionization threshold, defined as the field amplitude F needed to cause appreciable ionization in a fixed amount of time, is larger for "resonant" states $n_0 \simeq \omega^{-1/3}$ than for their immediate neighbors [2,5,6,9]. However, the initial state of the atom is not well-defined by the principal quantum number alone. Also, the state of the art ionization experiments lack selectivity with respect to the remaining quantum numbers [2]. Consequently, such experiments can only probe the atomic dynamics in the "ionizing" quantum number n_0: they average over the remaining dimensions of classical phase space in a more or less well-defined way. Probably for this reason, most of the theoretical studies of the problem have been so far dedicated to the interpretation of the quasi one-dimensional (1D) ionization process as suggested by the extremely rich experimental data [3], or to the justification of the underlying quasi one-dimensional picture on the grounds of the

---

[a] e-mail: `adb@mpq.mpg.de`

real, time dependent problem in a 2D configuration space (the third dimension being cyclic due to the azimuthal symmetry around the field polarization axis) [3,11].

Only recently there have been theoretical studies of the quantum dynamics of the real 3D Rydberg atom exploring all the dimensions of configuration space [12,13]. One major focus of this recent work was the characterization of individual states of the atom dressed by a microwave field which is resonant with the unperturbed Kepler motion. For some of these Floquet eigenstates (also known as eigenstates of the dressed atom), the probability density of the electron propagates in time along a classical periodic orbit of the system, being locked onto the external Kepler frequency. Such states have been baptized “non spreading wave packets”. They have been predicted more than 20 years ago [14], and some of their realizations have been described in 1D model systems [15]. However, the fact that the individual Floquet states have a wavepacket like time evolution was realized only later for linearly polarized microwaves [16,17]. Independently, a similar observation was made in circular polarization where Gaussian wave packets were shown to propagate almost without dispersion along circular periodic orbits [18]. References [19,20] identified the cause of this nondispersive evolution in the population of a wave packet eigenstate of the atom in the field.

It has also been observed that the non spreading wave packet eigenstates have extremely small individual ionization rates [16,17,19–21] making them behave like quasi-classical “quantum particles”. This is due to the fact that they are trapped inside a resonant island and can escape and ionize only *via* chaos assisted tunneling, *i.e.* tunneling outside the resonant island followed by chaotic diffusion towards the atomic continuum [20,21].

These wave packet states can be prepared by appropriate switching of the driving microwave field from a well-chosen initial atomic state [19,22], and their identification should be possible by spectroscopy of the Floquet energy spectrum [23,24] through a weak probe field, in analogy to the spectroscopy of dressed states in quantum optics [25]. However, for typical experimental field strengths, spectroscopy will detect a large number of narrow resonances, only few of them corresponding to nondispersive wave packet eigenstates. It is therefore desirable to have a precise estimate of the position of these particular states within the spectrum.

It is the purpose of the present contribution to provide an estimate for the energies of wave packet eigenstates, by the semiclassical quantization of the underlying classical dynamics of a Rydberg state driven by a resonant field of linear polarization. Such a study has already been performed for 1D atomic hydrogen [26] but it is of limited use for the real 3D dynamics of the atom. Similar but less involved calculations than those to follow have been presented earlier for the case of a resonant, circularly polarized field in either 2D [19] or 3D [20], and of a nonresonant, linearly polarized field [27].

The comparison with an exact quantum calculation will allow us to test the accuracy of the semiclassical prediction for the quasienergies. At the same time, we shall be able, as in the nonresonant case [27], to observe a neat signature of the classical dynamics in the ionization rates of the individual eigenstates (though locally disturbed due to quasidegeneracies with sublevels of adjacent Rydberg manifolds) in the near integrable regime. This signature is progressively destroyed as the classical excitation process turns chaotic. Finally, our present contribution also provides several classical trajectories along which non dispersive wave packets can be launched. In particular, we will show that non spreading wave packets propagating along a “true” Kepler ellipse (neither a circle, nor a straight line) can be populated using the $\omega = 2\omega_K$ resonance between the field and the unperturbed classical dynamics. It has been shown recently that similar states can be created by a combination of a $\omega = \omega_K$ resonant microwave field and of a static electric field [28].

2 Classical resonance approximation revisited

To perform the semiclassical quantization of the problem, we follow the classical picture of [29] further developed in [11]. The averaging method allows then to identify different time scales in the problem and split the dynamics into two weakly interacting one-dimensional motions. We refer the reader to the original papers for details, presenting below the main steps only. Consistently, the calculations presented here consider the effect of the microwave field as a perturbation of the field-free dynamics and only include the lowest non-vanishing order, which will be sufficient for quantitative interpretation of the quantum spectra, see Section 3. Extension of the same approach as to include a static electric field which enables the manipulation of the wavepacket trajectories is presented elsewhere [28].

The Hamiltonian of a Rydberg atom driven by a linearly polarized electromagnetic field writes, in the length gauge, using atomic units, neglecting relativistic effects, assuming an infinite mass of the nucleus, and employing the dipole approximation:

$$H = \frac{\mathbf{p}^2}{2} - \frac{1}{r} + Fz\cos(\omega t), \tag{1}$$

with the polarization vector of the field parallel to the z-axis.

To remove the explicit time dependence (necessary for the semiclassical quantization [30]) we first pass to the extended phase space [31], which comprises time as an additional generalized coordinate. The quasienergies will then be the quantum energy levels of the new Hamiltonian $\mathcal{H}$ defined by

$$\mathcal{H} = p_t + H, \tag{2}$$

with p_t the momentum canonically conjugate to time t. $\mathcal{H}$ is conserved during the temporal evolution of our system.

In the absence of the external field, the Kepler motion is integrable and traces a fixed (*i.e.* time-independent) elliptical trajectory. The associated action-angle variables are well-known. First, for the motion along the Kepler orbit they are I, the principal action (corresponding to the principal quantum number of the unperturbed hydrogen atom) and the canonically conjugate angle θ measuring the position of the electron along the Kepler ellipse. Then, the orientation of the Kepler ellipse in space is associated with two Euler angles ψ, canonically conjugate with the total angular momentum L, and φ, canonically conjugate with M, the z-component of the angular momentum. The angle ψ conjugate to L has a direct physical meaning: for $M = 0$, the case we shall focus on in the sequel (the extension to other M values being straightforward), it represents the angle between the Runge-Lenz vector $\mathbf{A}$ (oriented along the major axis) of the Kepler ellipse and the polarization vector of the field.

In these action-angle variables (I, θ), (L, ψ), (M, φ), we obtain [29]

$$\mathcal{H} = p_t - \frac{1}{2I^2} + \frac{F}{2}\sqrt{1-\frac{M^2}{L^2}}\sum_{m=-\infty}^{+\infty} V_m \times \left\{\cos(m\theta+\psi-\omega t)+\cos(m\theta+\psi+\omega t)\right\}, \tag{3}$$

with

$$V_m = \frac{I^2}{m}[J'_m(me) + \frac{\sqrt{1-e^2}}{e}J_m(me)],\ m \neq 0, \tag{4}$$

$$V_0 = -\frac{3}{2}eI^2, \tag{5}$$

$$e = \sqrt{1-\frac{L^2}{I^2}}, \tag{6}$$

where e is the eccentricity of the Kepler orbit of the Rydberg electron, and J_m, J'_m denote the Bessel functions and their derivatives, respectively. The absence of φ in the Hamiltonian reflects the azimuthal symmetry around the field axis and ensures the conservation of M.

In these new coordinates, the possible primary resonances between the Kepler motion and the driving field are immediately recognized: any time the frequency of the driving field matches a harmonic of the unperturbed motion, $s\theta - \omega t \simeq$ *constant*, the corresponding terms in the Fourier expansion (3) vary slowly and provide the major contribution to the sum over the Fourier index m. More precisely, following secular perturbation theory [31], a transformation to slowly varying variables

$$\hat{\theta} := \theta - \frac{\omega t}{s}, \quad \hat{I} := I, \quad \hat{p}_t := p_t + \frac{\omega I}{s}, \tag{7}$$

yields

$$\mathcal{H} = \hat{p}_t - \frac{1}{2\hat{I}^2} - \frac{\omega\hat{I}}{s} + \frac{F}{2}\sqrt{1-\frac{M^2}{L^2}} \times \sum_{m=-\infty}^{+\infty} V_m \left\{\cos\left(m\hat{\theta}+\psi+(\frac{m-s}{s})\omega t\right) + \cos\left(m\hat{\theta}+\psi+(\frac{m+s}{s})\omega t\right)\right\}. \tag{8}$$

Note that, while in the original coordinates, the Hamiltonian (3) is time-periodic with the microwave period $T = 2\pi/\omega$, the change of coordinates produces the Hamiltonian (8) periodic with period $\tau = sT$. This will become important for the semiclassical quantization below.

In the next step, we average $\mathcal{H}$ over the fast variable t (*i.e.* over one period τ), and we are left with the secular Hamiltonian

$$H_{secular} = \hat{p}_t - \frac{1}{2\hat{I}^2} - \frac{\omega\hat{I}}{s} + \frac{F}{2}\{V_s\cos(s\hat{\theta}+\psi) + V_{-s}\cos(s\hat{\theta}-\psi)\}, \tag{9}$$

which generates the secular (*i.e.* slow) evolution of the electron's trajectory under the external driving. After the further substitutions

$$\chi_s(L,\psi) := \frac{1}{2}\sqrt{V_s^2 + 2V_sV_{-s}\cos(2\psi) + V_{-s}^2}, \tag{10}$$

$$\tan\beta_s(L,\psi) := -\frac{V_s - V_{-s}}{V_s + V_{-s}}\tan\psi \tag{11}$$

we obtain the compact form

$$H_{secular} = \hat{p}_t - \frac{1}{2\hat{I}^2} - \frac{\omega\hat{I}}{s} + F\chi_s\cos(s\hat{\theta}-\beta_s). \tag{12}$$

The above procedure is valid at first order in F. Higher order expansions, using, *e.g.*, the Lie algebraic transformation method [31], are possible. An example is given in [27] for the non-resonant case at second order. Consistently, at the lowest non-vanishing order, χ_s and β_s are constant, evaluated at the value of the resonant action:

$$\hat{I} = I_s = \left(\frac{\omega}{s}\right)^{-1/3}, \tag{13}$$

and are consequently functions of L and ψ only.

Although the secular Hamiltonian acts in a four-dimensional phase space $(\hat{I}, \hat{\theta}, L, \psi)$, the dynamics is rather simple because there are different time scales, which implies an adiabatic separability in the spirit of the Born-Oppenheimer approximation. The shortest time scale is the Kepler period, already eliminated by passing to the secular Hamiltonian. This is valid only close to the resonance zone, *i.e.* for $\hat{I}$ close to I_s. Thus we can expand the Hamiltonian, equation (12), around the centre of the resonance island, *i.e.* in powers of $\hat{I} - I_s$. This gives, at second order, a standard pendulum Hamiltonian whose "gravitational field" scales as $F\chi_s(L,\psi)$. Hence, we expect the period of the motion in $(\hat{I}, \hat{\theta})$ to be of the order of $1/\sqrt{F\chi_s(L,\psi)}$. This is the second scale. For the motion in the (L, ψ) plane, the equations for the evolution of L and ψ, generated with the secular Hamiltonian, are obviously such that *both* dL/dt and $d\psi/dt$ are proportional to F. Hence, the period of the (L, ψ) motion will typically be of the order of $1/F$, much longer than the one of the fast motion in $(\hat{I}, \hat{\theta})$. This allows for the adiabatic separation of the variables. The adiabatic constant of the motion is $\chi_s(L,\psi)$ itself. The fast motion in the $(\hat{I},\hat{\theta})$ plane is thus similar to a pendulum with constant gravitational field proportional to this adiabatic constant, a problem which can be completely solved. There are librational modes where the Rydberg electron is trapped in the resonance island and rotational modes where the electron escapes the resonance island. The motion in the (L,ψ) plane follows curves of constant $\chi_s(L,\psi)$, at a velocity which depends on the average over the fast variables. The size of the resonance island in $(\hat{I},\hat{\theta})$ is determined by the characteristics of the motion in L and ψ. As we shall show below, these characteristics may strongly depend on the resonance number s. Finally, let us mention that this approach using adiabatic separability was used in [11,32] to estimate the ionization thresholds with the help of the Chirikov overlap criterion.

Before proceeding with the semiclassical quantization, we take advantage of the scaling properties of the classical dynamics [33], by virtue of the substitutions

$$H_{sc,0} := \lambda H_{sc}, \tag{14}$$

$$\hat{I}_0 := \lambda^{-1/2}\hat{I}, \tag{15}$$

$$L_0 := \lambda^{-1/2}L, \tag{16}$$

$$F_0 := \lambda^2 F, \tag{17}$$

$$\chi_{s,0} := \lambda^{-1}\chi_s, \tag{18}$$

$$\omega_0 := \lambda^{3/2}\omega, \tag{19}$$

$$t_0 := \lambda^{-3/2}t, \tag{20}$$

with λ being an arbitrary positive scaling factor. The common choice [2,3] is

$$\lambda = -\frac{1}{2E} = n_0^2, \tag{21}$$

where E is the initial energy of the electron with principal quantum number n_0. We adopt the same scaling below.

3 Semiclassical versus quantal results

The approximate separability of the temporal evolution in angular momentum and principal action makes the semiclassical quantization of our problem quite straightforward. In fact it constitutes a direct application of the semiclassical theory of periodically driven quantum systems as described in [30].

To find the semiclassical quasienergies of the Floquet eigenstates, we use the EBK quantization rules for $H_{secular}$, which, because of the adiabatic separability discussed above, reduce to the well-known WKB quantization rules in the $(\hat{I},\hat{\theta})$ and (L,ψ) planes. Indeed, with the standard quantization rule, the classical quantity p_t has to be replaced by $(1/i)(\partial/\partial t)$. The quantum operator generated from $\mathcal{H}$ with this quantization rule and periodic boundary conditions in time is nothing but the standard Floquet Hamiltonian [13] whose eigenvalues are the quasienergies of the Floquet eigenstates. In the secular approximation – as discussed above – we can use $H_{secular}$ instead of the full $\mathcal{H}$.

The $(\hat{p}_t,t)$ motion is easily quantized because the time variable is absent in equation (12): hence $\hat{p}_t$ remains constant. Using the periodicity in time, one finds:

$$\frac{1}{2\pi}\int_0^\tau \hat{p}_t\, dt = \frac{\hat{p}_t\tau}{2\pi} = k, \tag{22}$$

where, recall, $\tau = 2s\pi/\omega$ is the period of (8). The above quantization condition thus yields an additive term equal to $k\omega/s$ in the semiclassical energy, with k an arbitrary integer. Hence, semiclassically, the spectrum associated with the states localized in the s resonance island repeats itself along the energy axis at distances ω/s. We shall come back to this interesting point below, when discussing the specific case of the $s = 2$ resonance.

Taking advantage of the different time scales of the $(\hat{I},\hat{\theta})$ and the (L,ψ) motion [11], one can quantize the classical dynamics in the spirit of the Born-Oppenheimer approximation. We first quantize the fast $(\hat{I},\hat{\theta})$ motion, keeping L and ψ fixed, according to

$$\frac{1}{2\pi}\oint_\kappa \hat{I}d\hat{\theta} = q + \frac{\nu}{4}, \tag{23}$$

where κ is the closed classical trajectory in the $(\hat{I},\hat{\theta})$ plane. This yields the semiclassical energy spectrum as a continuous function of the $\chi_s(L,\psi)$ parameter. The final step is to perform the quantization of the (L,ψ) motion:

$$\frac{1}{2\pi}\oint_\gamma L d\psi = p + \frac{\mu}{4} \tag{24}$$

where γ stands for the closed classical trajectory in the (L,ψ) plane. This provides the desired discrete quasienergy levels $E_{p,q} + k\omega/s$, with p, q, k three integers. μ and ν are the Maslov indices [34] along the classical trajectories considered.

As we describe resonantly driven states, κ is chosen inside the resonance island in the $(\hat{I},\hat{\theta})$ plane. The position of the island is determined by the value of ω and by the choice of the order s of the resonance. For $s = 1$, *e.g.*, we will choose $\omega = 1/(21)^3$ such that the island is centered around $\hat{I} = n_0 = 21$.

In practice, we first quantize the motion in the (L,ψ) plane, equation (24), determined by χ_s. The quantized values of χ_s are then plugged into equation (23), what allows to proceed with the quantization in the $(\hat{I},\hat{\theta})$ plane. As, in both quantization equations, χ_s is a constant, we can apply the two quantization rules in any order we wish.

For comparison with the semiclassical results, the exact quantum mechanical quasienergies together with the associated ionization rates have been obtained by numerical diagonalization of the full Floquet Hamiltonian $\mathcal{H}$, beyond the secular approximation. The details of the method which also allows for the representation of the associated wave functions [35], are described in [13]. In short, the atomic part of the Hilbert space is represented by a Sturmian basis set, and complex scaling is used to treat the

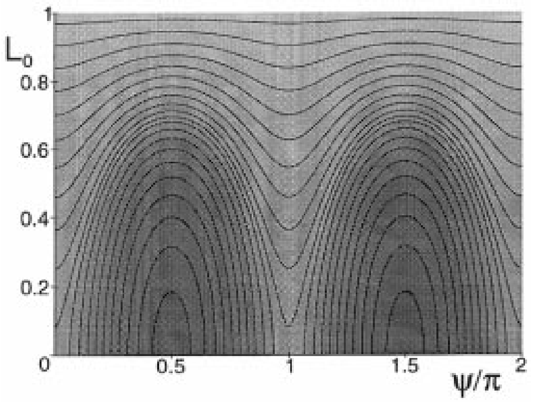

Fig. 1. Equipotential curves of the angular part χ_1 of the secular Hamiltonian $H_{secular}$ representing the slow evolution of the Kepler ellipse followed by a Rydberg electron, under the influence of a linearly polarized microwave field in resonance with the Kepler frequency of the electronic motion, represented in the plane of the L_0 and ψ coordinates. L_0 represents the total angular momentum (scaled such that a circular trajectory has $L_0 = 1$) and ψ the canonically conjugate angle measuring the angle between the axis of the field polarization and the major axis of the Kepler ellipse. The separatrix emanating from the unstable fixed point ($L_0 = 0, \psi = 0$) separates rotational and librational motions, both "centered" around their respective stable fixed points ($L_0 = 1$, ψ – arbitrary) and ($L_0 = 0$, $\psi = \pi/2$). The former corresponds to a circular orbit centered around the nucleus and lying in the plane containing the field polarization axis. For such a circular orbit, the direction of the Runge-Lenz vector is not defined, thus ψ is arbitrary. The second stable fixed point represents a straight linear orbit perpendicular to the field axis. The unstable fixed point corresponds to straight linear motion along the polarization axis. However, this initially degenerate Kepler ellipse will slowly precess in the azimuthal plane. The equipotential curves shown here are those satisfying the quantization condition (24), for $n_0 = 21$ and $p = 0 \dots 20$. The motion in the (L_0, ψ) plane is independent of F_0, in our first order treatment.

coupling to the continuum accurately. The quasienergies obtained are of the form $\epsilon_j = E_j - i\Gamma_j/2$, where E_j gives the real part of the quasienergy (defined modulo ω) while Γ_j is the width (ionization rate) of the eigenstate of the atom in the field.

3.1 1:1 resonance

Let us consider first the case $s = 1$, *i.e.* microwave frequencies $\omega \simeq \omega_K = 1/n_0^3$, or $\omega_0 = 1$. This is a case of particular interest for the construction of nonspreading wave packets [16–20,23,28,36]. We choose $n_0 = 21$ which is a reasonable compromise between the requirement of being in the semiclassical (large n_0) regime on the one hand, and the size of the Floquet matrix to be diagonalized on the other hand.

Figure 1 shows the equipotential curves of χ_1 in the (L_0, ψ) plane which are used as closed loops γ for the semiclassical quantization, equation (24). In fact, for a comparison with quantal data, the equipotential lines plotted correspond to the quantized values of χ_1 for $n_0 = 21$. There are librational orbits with stable fixed points at $L_0 = 0$ and $\psi = \pi/2, 3\pi/2$, representing a straight line orbit perpendicular to the field direction. Because of the azimuthal symmetry, these two points are equivalent. The orbit actually corresponds to motion with maximal radial component of the Runge-Lenz vector $\mathbf{A}$, *i.e.* $A_\rho = 1$. The rotational orbit with $L_0 = 1$ corresponds to a stable circular orbit centered around the nucleus, in a plane containing the field polarization axis. An alternative representation of the (L, ψ) motion on the unit sphere, spanned by L and the z and ρ-components of the Runge-Lenz vector, contracts the equipotential line representing this orbit in Figure 1 to another elliptic fixed point [27] with a surrounding librational motion. In both cases, the appropriate choice of the Maslov index in equation (24) is $\mu = 2$. The straight line orbits along the field polarization axis correspond to the unstable fixed points $L_0 = 0$, $\psi = 0, \pi$ ($A_z = 1$), defined by the self-intersection of the separatrix between rotational and librational modes.

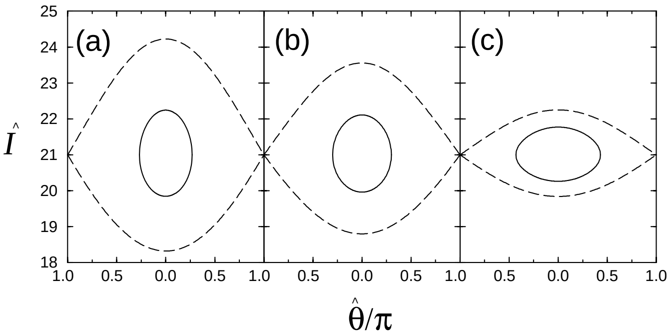

Fig. 2. Equipotential curves of the secular Hamiltonian $H_{secular}$ describing the motion of a Rydberg electron in a resonant microwave field, in $(\hat{I}, \hat{\theta})$ coordinates, corresponding to the atomic principal quantum number and the polar angle of the electron on the Kepler ellipse, respectively. The scaled microwave amplitude is $F_0 = 0.03$. Since the equipotential lines of $H_{secular}$ depend on the transverse motion in L_0 and ψ *via* the constant value of χ_1 only (corresponding to a fixed quantum number p of the transverse motion), contours (solid lines) are shown for 3 characteristic values of χ_1. Only the orbit satisfying (23) with $q = 0$, for $n_0 = 21$, is shown, together with the separatrix separating librational from rotational motion in the $(\hat{I}, \hat{\theta})$ plane. The separatrix defines the size of the principal resonance between the atom and the field. Panel (a) corresponds to the orbit with $L_0 \simeq 1$ (rotational orbit, $p = 20$), panel (b) to the orbit close to the separatrix of the angular motion ($p = 10$), panel (c) to the librational orbit close to the stable fixed point $L_0 = 0$, $\psi = \pi/2$. Note that the resonance island is smallest for librational, largest for rotational, and of intermediate size for separatrix modes of the angular motion.

Once the value of χ_1 along one of the trajectories of Figure 1 has been determined under these premises, we can perform the quantization of the $(\hat{I}, \hat{\theta})$ motion with the quantized value of χ_1. Figure 2 shows the equipotential lines of $H_{secular}$, for the three values of χ_1 corresponding to the stable circular, as well as to the stable and

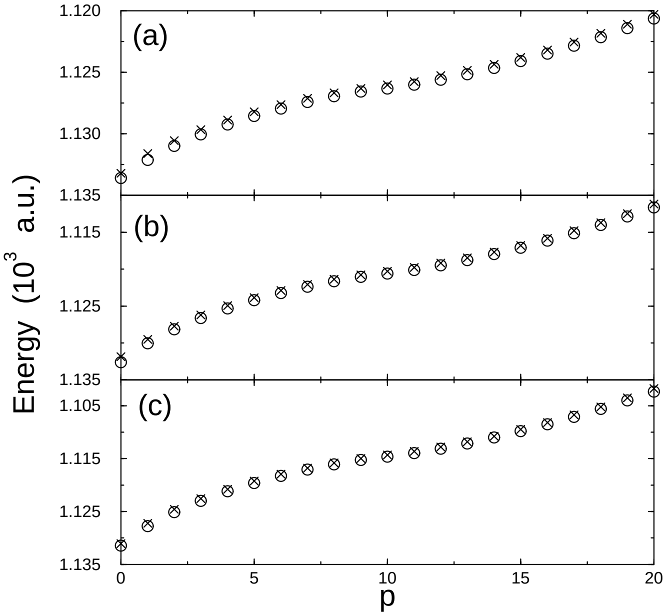

Fig. 3. Comparison of the semiclassical quasienergies (circles) originating from the unperturbed $n_0 = 21$ manifold (*i.e.* with $q = 0$, see Eq. (23)) with the exact quantum values (crosses), at different values of the (scaled) driving field amplitude $F_0 = 0.02$ (a), 0.03 (b), 0.04 (c). The agreement is excellent. The semiclassical quantum numbers $p = 0 \dots 20$ label the quantized classical trajectories plotted in Figure 1, starting from the librational state $|p = 0\rangle$ at lowest energies, rising through the separatrix states $|p = 10\rangle$ and $|p = 11\rangle$ to the rotational state $|p = 20\rangle$.

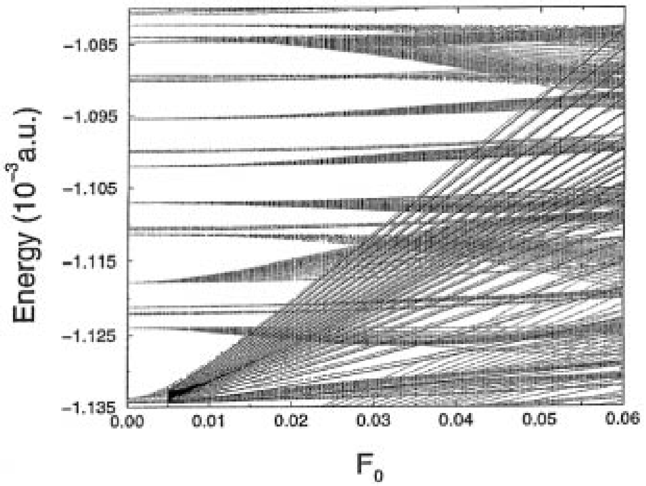

Fig. 4. Level dynamics of the exact quantum quasienergies (dotted lines) in the vicinity of the resonant manifold emerging from $n_0 = 21$ ($q = 0$), compared to the semiclassical prediction (full lines), for $F_0 = 0 \dots 0.06$. Note that the maximum field amplitude exceeds the typical ionization thresholds measured in current experiments at the principal resonance $\omega \simeq \omega_K$. Nonetheless, the semiclassical prediction accurately tracks the exact solution across a large number of avoided crossings, either with side bands of distant Rydberg levels, or with the adjacent Rydberg manifolds $n_0 = 20$ and $n_0 = 22$ (mixed by the microwave field) entering the plot from below.

the unstable straight line orbits, respectively. In each case the contour for the lowest state $q = 0$ has been drawn, together with the separatrix between librational and rotational $(\hat{I}, \hat{\theta})$ motion. The separatrices determine the size of the principal resonance island for the different substates of the transverse motion. Note that the principal resonance is largest for the stable circular orbit, whereas the weakest coupling in $\hat{I}$ is obtained in the vicinity of the straight line orbit perpendicular to the field axis. In fact, for this latter orbit itself, the first order coupling vanishes entirely. This shows that the semiclassical results obtained from our first order approximation (in F) of the Hamiltonian may be quite inaccurate in the vicinity of this orbit. Higher order corrections may be important.

As shown above, the classical motion in the (L, ψ) plane is slower than in the $(\hat{I}, \hat{\theta})$ plane. Hence, it is expected that states with the same q quantum number, but successive p quantum numbers will lie at neighboring energies, building manifolds. The energy spacing between states in the same manifold should scale as F_0 while the spacing between manifolds should scale as $\sqrt{F_0}$. The quantum calculations fully confirm this point of view, the manifolds originating from the degenerate hydrogenic energy levels at $F_0 = 0$.

We first concentrate on the $q = 0$ manifold, originating from the $n_0 = 21$ hydrogenic states. Figure 3 shows the comparison between the semiclassical and the quantum energies, for different values of the scaled driving field amplitude $F_0 = F n_0^4$. The agreement is excellent, except for the lowest lying states in the manifold for $F_0 = 0.02$. The energy level lowest in energy ($p = 0$) corresponds to a motion close to the stable fixed point $L_0 = 0$, $\psi = \pi/2$ in Figure 1; the highest energy level ($p = 20$) corresponds to the rotational motion $L_0 = 1$. The levels with the smallest energy difference ($p = 10, 11$) correspond to the librational and the rotational trajectories closest to the separatrix, respectively. The narrowing of the level spacing in their vicinity is just a consequence of the slowing down of the classical motion [37].

Figure 4 shows a global comparison of the semiclassical prediction with the exact level dynamics (energy levels *vs.* F_0), in a range from $F_0 = 0$ to $F_0 = 0.06$, which exceeds the typical ionization threshold ($F_0 \simeq 0.05$) observed in current experiments [2,13]. We observe that the semiclassical prediction accurately tracks the exact quasienergies, except in the region of very small F_0 where the size of the resonance island in $(\hat{I}, \hat{\theta})$ space is very small. Particularly impressing is the fact that, except at avoided crossings, the agreement is quite good even in regions where the resonant $n_0 = 21$ manifold overlaps with adjacent Rydberg manifolds, or with side bands of lower or higher lying Rydberg states.

The semiclassical construction of the energy levels from classical orbits is – necessarily – reflected by the localization properties of the associated eigenstates, as demonstrated by the electronic densities of the states $|p = 0\rangle$, $|p = 10\rangle$, and $|p = 20\rangle$ in Figure 5, for the same

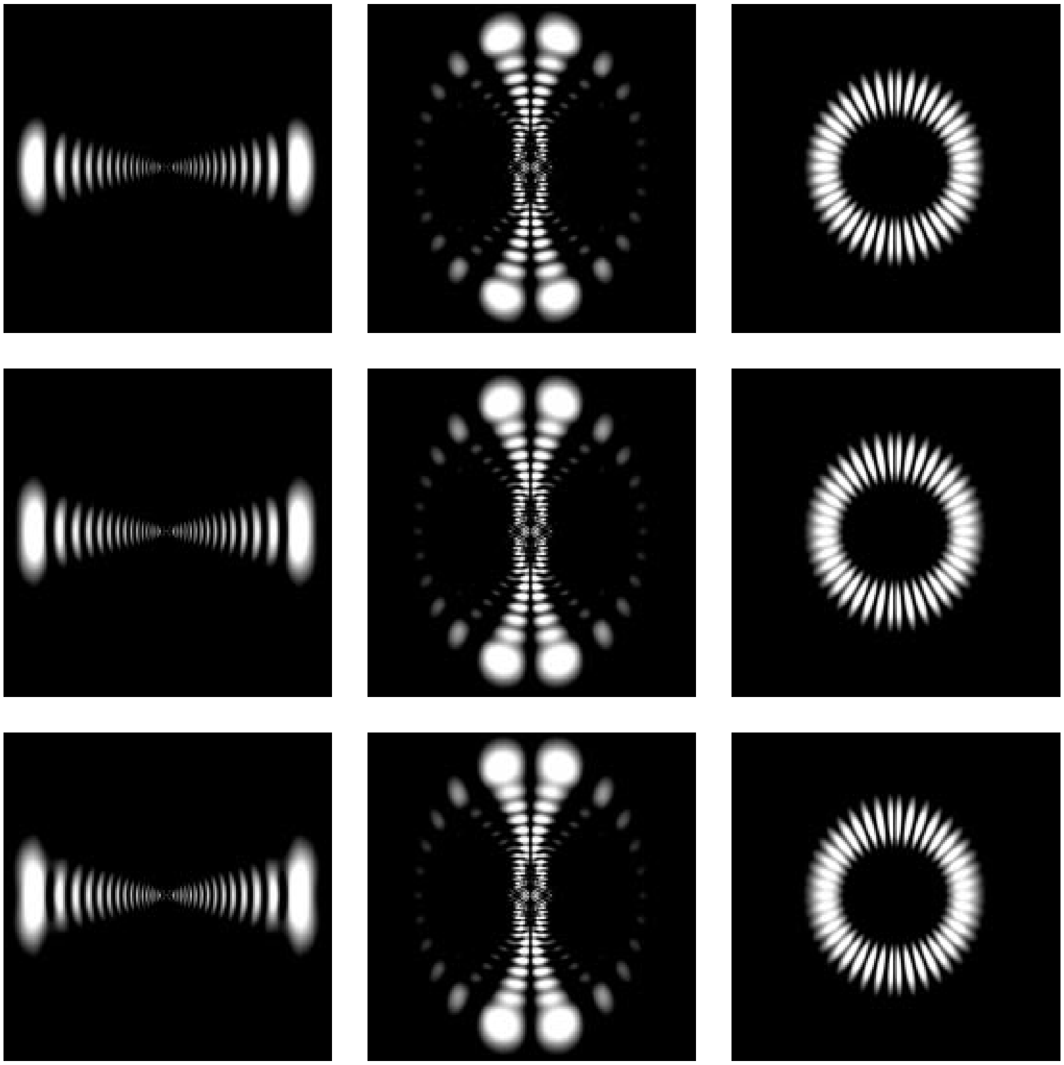

Fig. 5. Electronic densities of the extremal librational ($p = 0$, left), the separatrix ($p = 10$, center), and the extremal rotational ($p = 20$, right) quasienergy states in cylindrical coordinates (ρ, z), at different values of the driving field amplitude $F = 0.02$ (top), 0.03 (middle), 0.04 (bottom), averaged over one period of the driving field. Note the clear localization along the classical orbits corresponding to the respective contours in Figure 2, for *all* field amplitudes. The nodal lines of the electronic densities clearly exhibit the direction of the underlying classical motion. Each box is ± 1000 Bohr radii in both ρ and z directions. The microwave polarization axis along z is in the vertical direction of the figure.

field amplitudes as in Figure 3. Their localization along the classical orbits defined by their respective (un)stable fixed points is obvious [27]. Note in particular the nodal structure of the state $|p = 10\rangle$, associated with the unstable fixed point: there are sharp nodal lines perpendicular to the z-axis, reflecting the dominant motion along the z-axis, but also nodal lines of low visibility in the angular direction. They are a manifestation of the slow classical precession of the Kepler ellipse, *i.e.* the slow secular evolution in the (L, ψ) plane. The quantum state, however, dominantly exhibits the motion along the z-axis, as a signature of the effective separation of time scales of the radial and the angular motion, which was used above to deduce the secular Hamiltonian $H_{secular}$ [23]. It should be realized that the quasiclassical localization properties of the eigenstates are essentially unchanged as F rises, despite various avoided crossings which occur at intermediate field values, as obvious from Figure 4.

In contrast, Figures 6 and 7 show the evolution of the ionization rates of the individual substates of the resonant manifold $q = 0$ ($n_0 = 21$), in linear and logarithmic scales, respectively. At low amplitudes (*e.g.* $F_0 = 0.02$) the rates exhibit a largely unambiguous signature of the localization of the eigenstates and of the underlying classical dynamics, with extremal states being very stable while the states near the separatrix $p \simeq 10$ ionize faster. The slight shift to higher p values is in nice agreement with classical resonance analysis [32] indicating that elliptical orbits of high eccentricity are most vulnerable to microwave perturbation. This shows the limitations of the well-known 1D model; for an extended discussion, see [32]. The enhancement of the widths in the vicinity of the unstable fixed point is another manifestation of the stabilizing effect of classical structures surrounding stable periodic orbits. Only locally in the control parameter F, isolated avoided crossings of individual substates of the manifold ($p = 0$ and 19 in Fig. 7 at $F_0 = 0.02$) with adjacent Rydberg levels or sidebands of more distant states may perturb this picture, by enhancing the rate of the state which undergoes the avoided crossing (see also Fig. 4) [21]. However, at higher field strengths where the classical dynamics turns chaotic, the various states are strongly mixed with adjacent manifolds and the rates loose their specificity. That explains the almost flat distribution of the rates over the

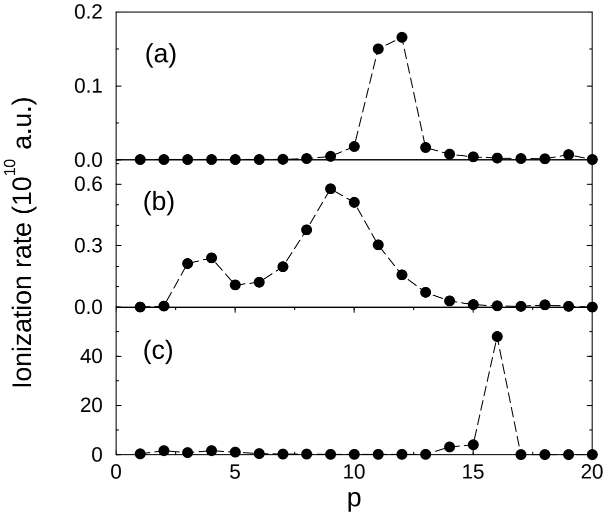

Fig. 6. The ionization rates of the states shown in Figure 3. While for small F_0, the rates change significantly over the manifold with a maximum in the vicinity of the separatrix states, this specificity of rates with respect to the classical motion is lost for most of the states at higher F_0, despite them being associated with the ground state $q = 0$ of the $(\hat{I}, \hat{\theta})$ resonance island and therefore remaining localized along the quantized (L, ψ) trajectories – as suggested by the excellent agreement of semiclassics and quantal quasienergies in Figure 3.

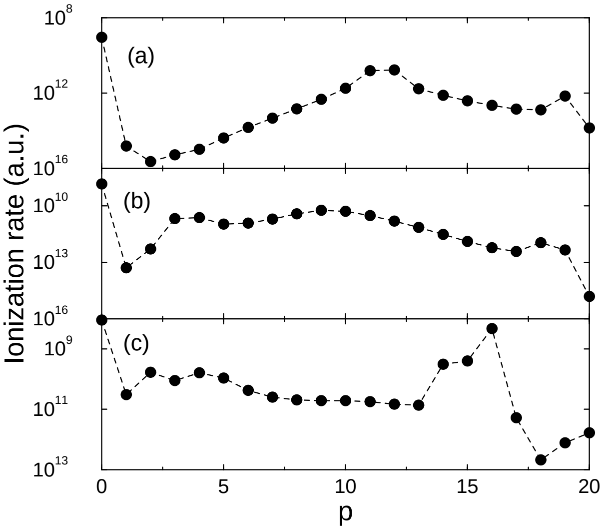

Fig. 7. Same as Figure 6, but on a logarithmic scale for the ionization rates.

manifold, at $F_0 = 0.04$ (with however, large fluctuations related to chaos assisted tunneling as explained in [21]). This observation of a transition from (L, ψ) *specific* (tunneling) rates (out of the resonance island) *below* the chaos transition to *nonspecific* rates at driving amplitudes *above* this transition explains the quasi one-dimensional appearance of the experimentally measured ionization thresholds [2].

We already mentioned earlier that the eigenstates displayed here are localized along classical trajectories which are resonantly driven by the external field. Hence, we should expect them to exhibit wave packet like motion along these trajectories, as the phase of the driving field is changed. This is shown in Figure 8 for the state $p = 20$ with maximal angular momentum $L_0 = 1$ [23,36]. Due to the azimuthal symmetry of the problem, the wave packet is actually a doughnut moving periodically from the north to the south pole (and back) of a sphere, slightly deformed along the field direction. The interference resulting from the contraction of this doughnut to a compact wave packet at the poles is clearly visible at phases $\omega t = 0$ and $\omega t = \pi$ in the plot. Note that the creation of unidirectional wave packet eigenstates moving along a circle in the plane containing the field polarization axis is not possible for the real 3D atom, as opposed to the reduced 2D problem studied in [36], due to the abovementioned azimuthal symmetry.

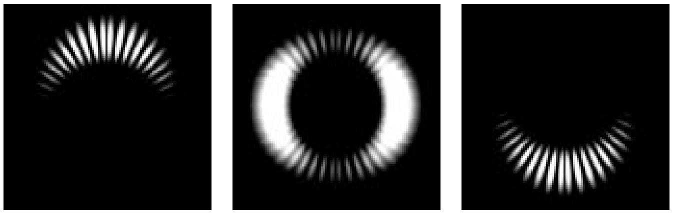

Fig. 8. Temporal evolution of the electronic densities for the extremal rotational quasienergy state $|p = 20\rangle$ of the $n_0 = 21$ resonant manifold, for different phases $\omega t = 0$ (left), $\omega t = \pi/2$ (center), $\omega t = \pi$ (right) of the driving field, at amplitude $F_0 = 0.03$, represented in cylindrical coordinates. Each box is $\pm\,700$ Bohr radii in both ρ and z directions. The state actually represents a nondispersing wave packet shaped like a doughnut, moving periodically from the north to the south pole (and back) of a sphere. For higher n_0, the longitudinal localization along the circular orbit should become better and better. The microwave polarization axis along z is in the vertical direction of the figure.

For other states in the $n_0 = 21$ resonant manifold, the longitudinal localization along the periodic orbit is less visible. The reason is that χ_1 is smaller than for the $p = 20$ state, leading to a smaller resonance island in $(\hat{I}, \hat{\theta})$ and consequently to less efficient localization. Going to higher n_0 values should improve the situation.

Let us finally briefly discuss "excited" states in the principal action island, *i.e.* manifolds corresponding to $q > 0$ in equation (23). Figure 9 shows the quantal level dynamics with the semiclassical prediction for $q = 1$ superimposed. The states in this manifold originate from $n_0 = 22$. We observe quite good agreement between quantal and semiclassical regime for *higher* lying states in the manifold (for which the principal action island is large). For lower lying states the agreement is reached for higher values of F_0. If F_0 is too low, the states are not fully localized inside the resonance island (which, due to its size may contain a single state only, with $q = 0$) and, consequently, are badly reproduced by the resonant semiclassical approximation. This is further exemplified in Figure 10 where the case $q = 2$ is shown. Here, the agreement is much worse than for smaller values of q and is observed only for large F_0 and large p. This confirms the picture

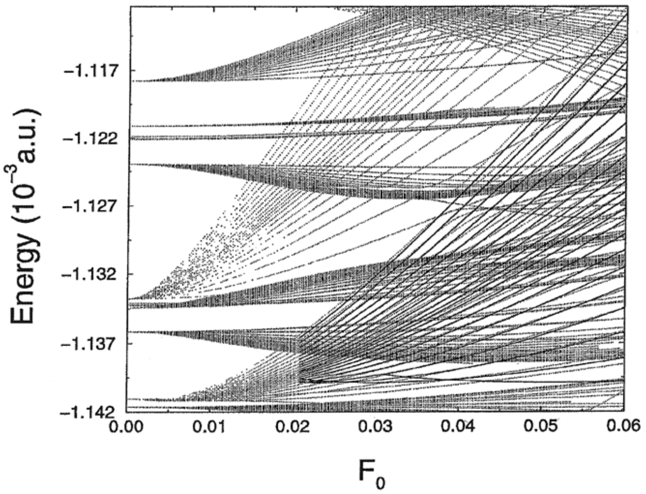

Fig. 9. Comparison of the exact quantum level dynamics (dotted lines) of states originating (at $F_0 = 0$) from the $n_0 = 22$ ($q = 1$) manifold with the semiclassical prediction obtained from quantizing the classical motion within the resonance island. For sufficiently high F_0, these quantum states are captured by the principal resonance island and correspond semiclassically to the first excited state of the motion in the $(\hat{I}, \hat{\theta})$ plane, *i.e.* $q = 1$ in equation (23). Since the island size depends on the (L, ψ) angular motion (value of p in Eq. (24)), states with large p first enter the resonance zone. For them good agreement between quantum and semiclassical quasienergies is observed at lower F_0 values than for states with small p.

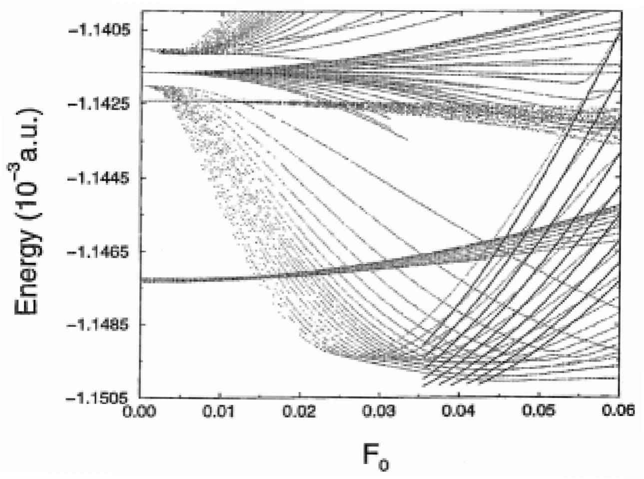

Fig. 10. Same as Figure 9, but for $q = 2$. The quantum states originate from the manifold $n_0 = 20$. The resonance island in $(\hat{I}, \hat{\theta})$ coordinates is too small to support some $q = 2$ states for $F_0 < 0.03$, as seen from the negative slope of the states. The quantum states "cross" the separatrix and successively enter the resonance zone, starting from the largest value of p in equation (24) (the resonance island size increases with p). Even for large $F_0 > 0.04$, only a minority of the states in the $n_0 = 20$ manifold is well-represented by the resonant semiclassical dynamics.

that the validity of the semiclassical approach presented is directly related to the size of the resonance island in the $(\hat{I}, \hat{\theta})$ space.

3.2 2:1 resonance

Consider now the $s = 2$ resonance, *i.e.* the case when the microwave frequency is twice as large as the Kepler frequency ($\omega \simeq 2\omega_K$). This situation may serve as an example of a general s:1 resonance. As for the $s = 1$ case, we first study and quantize the slow motion in the (L, ψ) plane. Figure 11 shows the corresponding equipotential lines of χ_2 in the (L, ψ) plane – calculated from equations (10, 4), *i.e.* completely expressible in terms of Bessel functions – (for a comparison with quantal data, the equipotential lines correspond to quantized values of χ_2 for $n_0 = 42$).

One immediately notices that the secular motion in this case is topologically different from that corresponding to the $s = 1$ resonance (compare with Fig. 1). Again, the unstable fixed points $L_0 = 0$, $\psi = 0, \pi$, corresponding to the straight line orbits parallel to the field polarization axis, are the origin of the separatrix dividing (L_0, ψ) space. Similarly, stable fixed points exist for $L_0 = 0$, $\psi = \pi/2$ and $L_0 = 0$, $\psi = 3\pi/2$, corresponding to the straight line orbit perpendicular to the polarization axis (as for $s = 1$, due to azimuthal invariance, this is really a single orbit or rather a family of equivalent orbits perpendicular to the polarization axis). Also, there is again a stable fixed point corresponding to the circular orbit (represented by the line $L_0 = 1$, arbitrary ψ).

However, there are also new fixed points: an unstable fixed point at $L_0 \simeq 0.77$, $\psi = \pi/2, 3\pi/2$ corresponding to unstable elliptical orbits with major axis perpendicular to the polarization axis, and two stable fixed points at $L_0 \simeq 0.65$, $\psi = 0, \pi$, which correspond to stable elliptical orbits with major axis parallel and antiparallel to the polarization axis. Importantly, for these new stable fixed points, the resonance island in $(\hat{I}, \hat{\theta})$ coordinates is quite large (as revealed by the light background designing large values of χ_2 in the grayscale plot of Fig. 11). Thus, the motion in the vicinity of these fixed points is strongly confined *both* in the angular coordinates (L_0, ψ) and in the $(\hat{I}, \hat{\theta})$ coordinates: the corresponding eigenstates should be nonspreading wave packets localized both longitudinally along the orbit (locked on the microwave phase) and in the transverse direction. Furthermore, note from equation (1) that $\psi = 0$ changes to $\psi = \pi$ (or z changes to $-z$) if we change F_0 to $-F_0$, that is if we shift the phase of the microwave by π. Consequently, for a given microwave field phase, the two stable points correspond to distinct classical dynamics.

By contrast, the other stable points, the circular orbit and the straight line orbits perpendicular to the polarization axis, lie in the minima – in fact, the zeroes – of χ_2. For the latter, the coupling vanishes at first order in F, exactly like in the case of the $s = 1$ resonance. Also, the circular orbit, which corresponds to a maximum of χ_1 (leading

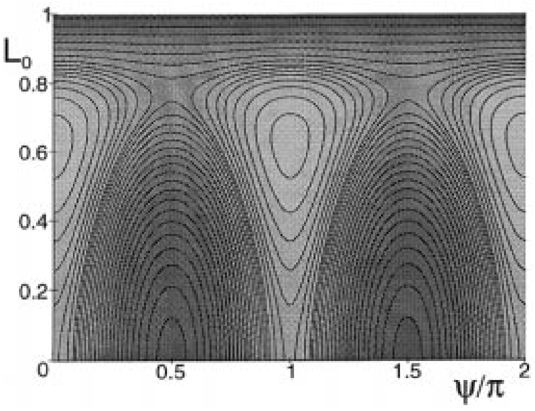

Fig. 11. Equipotential curves of the angular part χ_2 of the secular Hamiltonian $H_{secular}$. They represent the slow evolution of the classical Kepler ellipse followed by a Rydberg electron, exposed to a linearly polarized microwave whose frequency is twice the Kepler frequency of the unperturbed motion; the equipotential curves are plotted in the (L_0, ψ) plane. The light shaded regions correspond to maxima of χ_2, the dark shaded regions to minima of χ_2, and thus to the size of the resonance island in the $(\hat{I}, \hat{\theta})$ motion, by virtue of equation (12). The stable fixed points lie at extrema of χ_2. Note that, despite the rotational invariance of our problem in configuration space, the stable fixed points corresponding to elliptical trajectories at $L_0 \simeq 0.65$, $\psi = 0, \pi$ correspond to *distinct* classical dynamics. The equipotential curves shown here are those that satisfy the quantization condition (24), for $n_0 = 42$ and $p = 0 \ldots 41$. As in Figure 1, the motion in the (L_0, ψ) plane is independent of F_0.

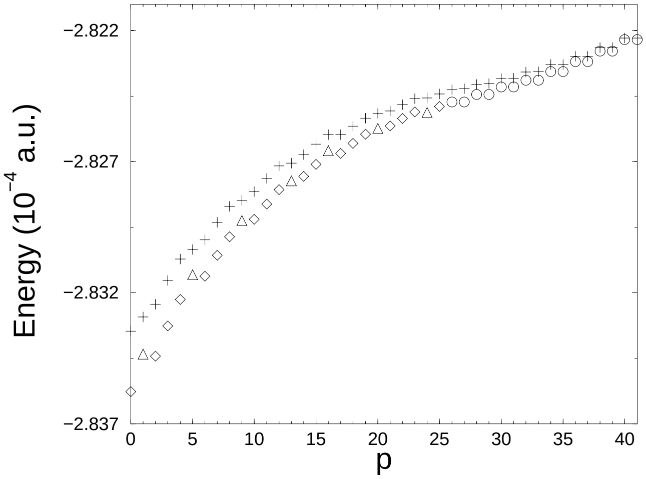

Fig. 12. Comparison of exact quasienergies of states originating from the $n_0 = 42$ manifold (depicted by pluses) with the semiclassical prediction based on the quantization of the $s = 2$ resonance island, for $F_0 = 0.04$. The results of the semiclassical quantization are depicted by open symbols. Circles correspond to doubly degenerate states localized in the vicinity of maxima of χ_2, around the elliptical fixed point at $L_0 \simeq 0.65$, $\psi = 0, \pi$ in Figure 11. Widely spaced triangles correspond to almost circular states in the vicinity of the stable minimum at ($L_0 = 1, \psi$ arbitrary), while diamonds correspond to states localized around the stable minimum at $L_0 = 0$, $\psi = \pi/2$ (and equivalently, due to the azimuthal invariance, $\psi = 3\pi/2$). Observe that the agreement between semiclassical and quantum energies is very good, provided the size of the resonance island in $(\hat{I}, \hat{\theta})$ coordinates is sufficiently large (high lying states in the manifold). For low lying states in the manifold the discrepancies between quantum results and semiclassical predictions are significant, due to the insufficient size of the island.

to strong localization in the $(\hat{I}, \hat{\theta})$ coordinates) defines a minimum of χ_2. The reason is simple: the motion on the circular orbit is purely harmonic and no coupling is possible for $\omega = 2\omega_K$. Thus we expect that the corresponding island in $(\hat{I}, \hat{\theta})$ space, appearing for trajectories close to the circular orbit, is quite small and localization in $\hat{\theta}$ not very effective, either.

To be able to clearly separate quantum states localized in different parts of the (L_0, ψ) phase space, and also to observe the details of the wavefunctions in more detail, we semiclassically quantize the classical motion in the $n_0 = 42$ resonant manifold (and not $n_0 = 21$ as for the $s = 1$ resonance), choosing the microwave frequency as:

$$\omega = 2\omega_K = \frac{2}{(42)^3} \cdot \tag{25}$$

A second reason to choose a higher n_0 value is the strength of the resonance coupling in equation (4), *i.e.* the possible values of χ_2. The coupling is significantly weaker than for $s = 1$, the maximum value of χ_2 being about 2.5 times smaller than the maximum value of χ_1, for the same values of F and unperturbed action (in other words, exciting the system at twice his internal frequency is less efficient than excitation at the internal frequency). Consequently, for the size of the resonance island in the $(\hat{I}, \hat{\theta})$ plane to be sufficiently large to capture quantum states, we either have to increase F_0 to values beyond the classical chaos border (which in principle invalidates the secular approximation), or to go to higher n_0.

Figure 12 shows a comparison between the semiclassical quantized quasienergy levels of the Floquet eigenstates with the quantum spectrum for the whole manifold $n_0 = 42$, *i.e.* $q = 0$ in equation (23), at $F_0 = 0.04$. Observe that the 16 highest lying states appear in 8 quasi-degenerate pairs differing by parity. Exact degeneracy does not happen because of tunneling effects: the lower the pair of states, the larger the energy splitting of the pair. The tunneling process involved here is a "tranverse" tunneling in the (L, ψ) plane, where the electron jumps from the $(L_0 \simeq 0.65, \psi = 0)$ Kepler elliptical trajectory to its image by z-parity, the $(L_0 \simeq 0.65, \psi = \pi)$ Kepler elliptical trajectory. It exists only because χ_2 has a specific form with two *distinct* maxima not lying at $\psi = \pi/2$.

The uppermost pair corresponds to states localized close to the fixed points $L_0 \simeq 0.65$, $\psi = 0, \pi$ and are non spreading wave packets (see below). For these states (large resonance island in the $(\hat{I}, \hat{\theta})$ space), the semiclassical quantization nicely agrees with the quantum results. On the other hand, the agreement between the quantum and the semiclassical results gets progressively worse for lower states in the manifold, when the size of the island in $(\hat{I}, \hat{\theta})$ coordinates becomes smaller. Still, even for the lowest states in the manifold, the disagreement between the semiclassical and quantum results is at most of the order of the spacing between adjacent levels. Below the energy of the unstable fixed points at $L_0 \simeq 0.77, \psi = \pi/2, 3\pi/2$ there are no more pairs of classical trajectories in the (L, ψ) plane corresponding to distinct classical dynamics related by z-parity. Hence, the quasi-degeneracy has to disappear, as confirmed by the exact quantum results shown in Figure 12. On the other hand, there are two regions of the (L, ψ) plane which can give quantized values of χ_2 (and consequently quasienergies) in the same range: the first one is around the stable fixed points ($L_0 = 0, \psi = \pi/2, 3\pi/2$) and the second one around the stable fixed point $L_0 = 1$. In the semiclassical quantization scheme, they are completely uncoupled, producing two independent non-degenerate series of energy levels. The first region has a larger area and consequently produces more states; the full spectrum looks rather complicated because of the interleaving of the two series.

Let us now address the existence of other "mirror" manifolds, separated in energy by $\omega/2 = \omega_K$ from the original manifold, which are expected on the basis of equation (22). This is a manifestation of the fact that the periodicity of the Hamiltonian (8) is $\tau = 2T = 4\pi/\omega$ rather than T, and is easy to understand classically. Consider the elliptical fixed point lying in the center of the 2:1 resonance zone. Its period is precisely τ, while there exists also a second, exact replica of the same trajectory, shifted in orbital phase by π. In other words, two (in phase space) identical classical trajectories exist which are *distinct* in *extended* phase space since one is shifted with respect to the other by T. This situation in fact closely resembles the motion of a particle in a double potential well. Classically, the motion is confined to one of the two wells, whilst the corresponding quantum states are the linear combinations of solutions in each well. They are almost degenerate, and their energy difference is a manifestation of quantum tunneling.

Here, similarly, a single non spreading wave packet (the analog of the state localized in one well) cannot build a stationary Floquet eigenstate. Indeed, after one microwave period (half a Kepler period), it has traveled only half of the Kepler ellipse and cannot return to the initial point: the solution is to use a combination of two such non spreading wave packets, shifted by π. As these two wavepackets are localized in different regions of phase space at the same time, they are coupled only by tunneling. This tunneling process is *completely* different from the "transverse" one in the (L, ψ) plane described above. We here have a "longitudinal" tunneling where the electron jumps from a location on a Kepler orbit to another location further on the *same* orbit. Since the shift between the two classical solutions occurs on the time axis, there is a semiclassical spacing in energy of $\omega/2$. The corresponding states should be quasi-degenerate modulo $\omega/2$ with the remaining difference due to quantum "longitudinal" tunneling [15]. It has to be stressed that this is a very general phenomenon in the vicinity of a s:1 resonance (with $s \geq 2$) due to the phase space structure in the $(\hat{I}, \hat{\theta})$ plane, in contrast with the "transverse" quasi-degeneracy due to the specific form of χ_2.

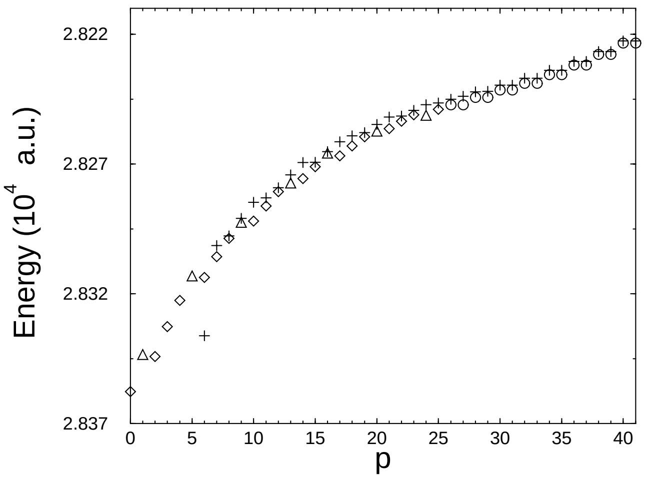

Fig. 13. Same as Figure 12, but for the "mirror" manifold shifted in energy by $\omega/2$. While, for most states, the agreement with semiclassics is of the same quality as in Figure 12, no quantum data are plotted at the bottom of the manifold. Indeed, at those energies, another Rydberg manifold strongly perturbs the spectrum due to close accidental degeneracy. Consequently, the unambiguous identification of individual states is very difficult.

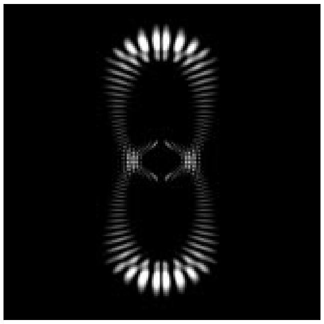

Fig. 14. Electronic density of the uppermost eigenstate of the $n_0 = 42$ manifold of Figure 12, averaged over one microwave field period. This state presents localization along a pair of Kepler ellipses elongated along the field polarization axis. The box is ± 3500 Bohr radii in both ρ and z directions. The microwave polarization axis along z is in the vertical direction of the figure.

Inspection of the quantum quasienergy spectrum at energies shifted from the original $n_0 = 42$ manifold by $\omega/2$, provides the manifold shown in Figure 13, together with the semiclassical prediction. Observe that the agreement between quantum and semiclassical quasienergies is similar to that observed in Figure 12, except for the low lying states. Here, incidentally, the states anchored to the resonance zone are strongly perturbed by another Rydberg manifold; proper identification of the individual quantum states is very difficult in this region.

We finally study the properties of the wave functions associated with the highest states in the manifolds of

Figures 12 and 13 (*i.e.* with the largest resonance island in $(\hat{I}, \hat{\theta})$ coordinates). These wave functions should localize in the vicinity of stable trajectories of period 2, *i.e.* they should be strongly localized both in angular and orbital coordinates, along an elliptical Kepler orbit of intermediate eccentricity.

However, because of the longitudinal quasi-degeneracy, we expect to have two wave packets on the ellipse exchanging their positions with period T. Also, because of the transverse quasi-degeneracy, we should also have combinations of the the elliptical orbits with $\psi = 0$ and $\psi = \pi$. Altogether, this makes four individual wavepackets for each Floquet state. Recall from the previously discussed case of the $s = 1$ resonance that a single wave packet appears as a counter propagating pair of two wave packets (or as a doughnut, see Fig. 8), due to azimuthal symmetry around the z-axis. Here, we thus expect a single Floquet wavefunction to be composed of 8 wave packets (or 4 doughnuts)!

The quantum calculations fully confirm this prediction. Figure 14 shows the electronic density of the upper Floquet state in the $n_0 = 42$ manifold, averaged over one field period. As expected, it is localized on the two symmetric Kepler ellipses but longitudinally delocalized because of the time average. In fact, there are 4 Floquet states displaying very similar electronic densities. These are the pair of upper states in the $n_0 = 42$ manifold and the pair of upper states in the "mirror" manifold discussed above.

Figure 15 shows the electronic densities of these 4 Floquet eigenstates for the phase $\omega t = 0$ of the driving field: the 4 doughnuts are now clearly visible, as well as the orbital and radial localizations along the two elliptical trajectories. Very much in the same way as for a double well potential, a linear combination of these four states allows for the selection of one single doughnut, localized along one single classical Kepler ellipse. This wave packet then evolves along this trajectory without dispersion, as demonstrated in Figure 16. Here, the temporal evolution of the electronic density is monitored by application of the time evolution operator generated by the Hamiltonian H [13] to the linear combination of Floquet eigenstates.

Note, however, that this simpler wave packet does not exactly repeat itself periodically, and consequently slowly disappears at long time, for at least two reasons: firstly, because of longitudinal and transverse tunneling, the phases of the 4 Floquet eigenstates will be a little different after one period which induces spreading, and secondly, the ionization rates of the individual Floquet states lead to ionization and loss of phase coherence, especially if the rates of the 4 states are not equal.

4 Conclusions

We have performed the semiclassical quantization of the motion of a resonantly driven Rydberg electron of atomic hydrogen. The semiclassical prediction turns out to predict the exact positions of the energy levels within a margin smaller than the average level spacing, for field

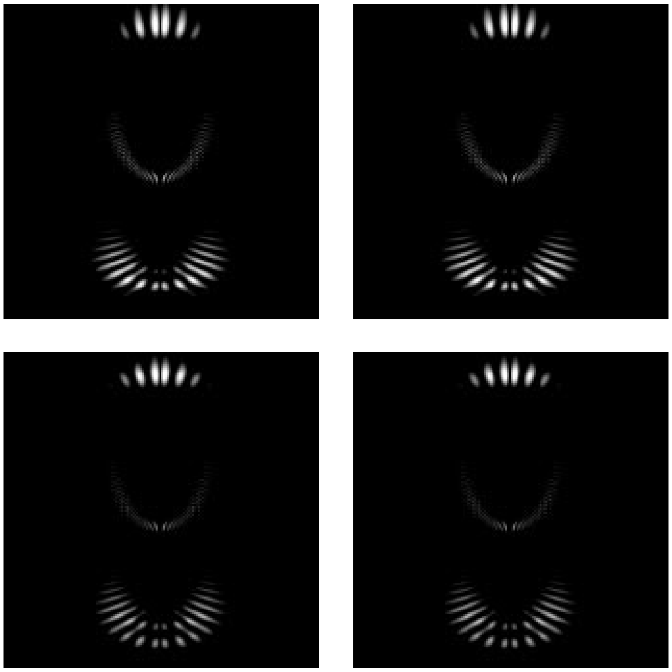

Fig. 15. Electronic densities of the eigenstates of the uppermost doublet states (top) of the $n_0 = 42$ manifold of Figure 12, and of their mirror states (bottom) shifted by $\omega/2$, at driving field phase $\omega t = 0$. Compared to Figure 14, one can see the longitudinal localization on the Kepler ellipses (similar for all states). On each ellipse, there are 4 different individual wave packets (or rather, due to the azimuthal symmetry, 2 doughnut wave packets) visible, which propagate along the Kepler ellipse. Notice the phase shift of π in the temporal evolution on the two ellipses, implied by z-inversion. The microwave polarization axis along z is in the vertical direction of the figure.

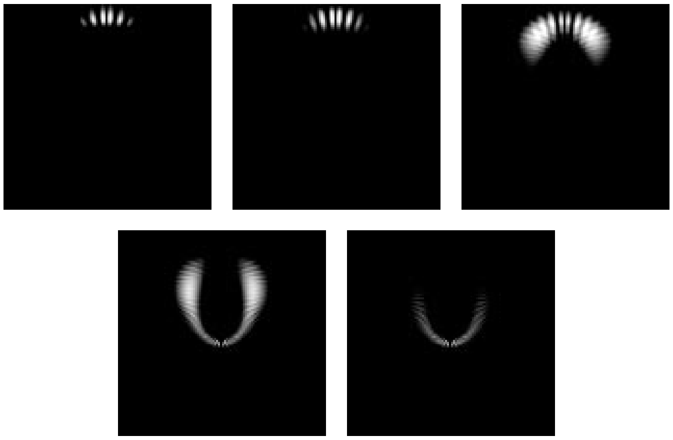

Fig. 16. Temporal evolution of the convenient linear combination of the 4 states of Figure 15, for phases $\omega t =$ (top left) 0, (top center) $\pi/2$, (top right) π, (bottom left) $3\pi/2$, (bottom right) 2π of the driving field. Clearly, a single doughnut propagating along a single trajectory has been selected by the linear combination. This wave packet essentially repeats its periodic motion with period $4\pi/\omega$. It slowly disperses, either because the 4 building states are not exactly degenerate (tunneling effect) or because it ionizes. The microwave polarization axis along z is in the vertical direction of the figure.

strengths even beyond the experimental ionization threshold fields, at least for the principal nonlinear resonance between the driving field and the unperturbed classical motion, when $\omega \simeq \omega_K$. The transition from near regular to chaotic excitation in the principal action is clearly exhibited in the ionization rates of the sublevels of the resonantly driven Rydberg manifold, which are (L,ψ) specific in the near integrable regime but nonspecific beyond the chaos transition. Our semiclassical approach can be considered as a reliable tool for the identification of wave packet eigenstates, *e.g.* in Floquet spectroscopy type experiments [23].

K.S. is a fellow of the Foundation for Polish Science. K.S. and J.Z. acknowledge support by Polish Committee for Scientific Research (KBN) under grant 2P03B-00915. Polish-French collaboration has been supported by KBN and MRT/MAE *via* the Programme International de Coopération Scientifique (CNRS) no. 408 and by the bilateral collaboration scheme no. 76209. A.B. and D.D. acknowledge partial financial support by the French-German Procope program 97022. CPU time has been provided by IDRIS and RZG. Laboratoire Kastler-Brossel, de l'École Normale Supérieure et de l'Université Pierre et Marie Curie, is unité associée 18 du CNRS.

References

1. J.E. Bayfield, P.M. Koch, Phys. Rev. Lett. **33**, 258 (1974).
2. P.M. Koch, Physica D **83**, 178 (1995) and references therein.
3. G. Casati, B.V. Chirikov, D.L. Shepelyansky, I. Guarneri, Phys. Rep. **154**, 77 (1987); G. Casati, I. Guarneri, D.L. Shepelyansky, IEEE J. Quant. Electron. **24**, 1420 (1988).
4. S. Fishman, D.R. Grempel, R.E. Prange, Phys. Rev. Lett. **49**, 509 (1982).
5. E.J. Galvez, B.E. Sauer, L. Moorman, P.M. Koch, D. Richards, Phys. Rev. Lett. **61**, 2011 (1988).
6. J.E. Bayfield, G. Casati, I. Guarneri, D.W. Sokol, Phys. Rev. Lett. **63**, 364 (1989).
7. R. Blümel, A. Buchleitner, R. Graham, L. Sirko, U. Smilansky, H. Walther, Phys. Rev. A **44**, 4521 (1991).
8. M. Arndt, A. Buchleitner, R.N. Mantegna, H. Walther, Phys. Rev. Lett. **67**, 2435 (1991).
9. B.E. Sauer, M.R.W. Bellermann, P.M. Koch, Phys. Rev. Lett. **68**, 1633 (1992).
10. J.G. Leopold, D. Richards, J. Phys. B **27**, 2169 (1994).
11. J.G. Leopold, D. Richards, J. Phys. B **19**, 1125 (1986).
12. A. Buchleitner, D. Delande, Phys. Rev. Lett. **70**, 33 (1993); *ibid.* **71**, 3633 (1993).
13. A. Buchleitner, D. Delande, J.C. Gay, J. Opt. Soc. Am. B **12**, 507 (1995).
14. G.P. Berman, G.M. Zaslavsky, Phys. Lett. A **61**, 295 (1977).
15. J. Henkel, M. Holthaus, Phys. Rev. A **45**, 1978 (1992); M. Holthaus, Chaos, Solitons and Fractals **5**, 1143 (1995) and references therein.
16. A. Buchleitner, Ph.D. thesis, Université Pierre et Marie Curie, Paris, 1993 (unpublished).
17. D. Delande, A. Buchleitner, Adv. At. Mol. Opt. Phys. **35**, 85 (1994); A. Buchleitner, D. Delande, Phys. Rev. Lett. **75**, 1487 (1995).
18. I. Bialynicki-Birula, M. Kalinski, J.H. Eberly, Phys. Rev. Lett. **73**, 1777 (1994).
19. D. Delande, J. Zakrzewski, A. Buchleitner, Europhys. Lett. **32**, 107 (1995).
20. J. Zakrzewski, D. Delande, A. Buchleitner, Phys. Rev. Lett. **75**, 4015 (1995).
21. J. Zakrzewski, D. Delande, A. Buchleitner, Phys. Rev. E **57**, 1458 (1998); J. Zakrzewski, D. Delande, A. Buchleitner, Acta Phys. Polon. A **93**, 179 (1998).
22. J. Zakrzewski, D. Delande, J. Phys. B **30**, L87 (1997).
23. A. Buchleitner, D. Delande, J. Zakrzewski, in *Proceedings of the 7th International Conference on Multiphoton Processes*, edited by P. Lambropoulos, H. Walther (Institute of Physics Publishing, Bristol, 1997).
24. R. Blümel, U. Smilansky, J. Opt. Soc. Am. B **7**, 664 (1990).
25. C. Cohen-Tannoudji, J. Dupont-Roc, G. Grynberg, *Atom-Photon Interactions: Basic Processes and Applications* (John Wiley and Sons, New York, 1992).
26. L. Sirko, P.M. Koch, Appl. Phys. B **60**, S195 (1995).
27. A. Buchleitner, D. Delande, Phys. Rev. A **55**, 1585 (1997).
28. K. Sacha, J. Zakrzewski, D. Delande, Eur. Phys. J. D **1**, 231 (1998).
29. B.I. Meerson, E.A. Oks, P.V. Sasorov, J. Phys. B **15**, 3599 (1982).
30. H.P. Breuer, M. Holthaus, Ann. Phys. **211**, 249 (1991); see also B. Mirbach, H.J. Korsch, J. Phys. A **27**, 6579 (1994).
31. A.J. Lichtenberg, M.A. Lieberman, *Irregular and stochastic motion* (Springer-Verlag, New York, 1993).
32. K. Sacha, J. Zakrzewski, Phys. Rev. A **56**, 719 (1997).
33. I.C. Percival, Proc. Roy. Soc. Lond. A **353**, 289 (1977).
34. A. Ozorio de Almeida, *Hamiltonian Systems and Quantization* (Cambridge University Press, Cambridge, 1989).
35. A. Buchleitner, B. Grémaud, D. Delande, J. Phys. B **27**, 2663 (1994).
36. M. Kalinski, J.H. Eberly, Phys. Rev. A **52**, 4285 (1995).
37. D. Delande, J. Zakrzewski, A. Buchleitner, Phys. Rev. Lett. **79**, 3541 (1997).